

Tunable SiO2 to SiOxCyH films by ozone assisted chemical vapor deposition from tetraethylorthosilicate and hexamethyldisilazane mixtures

Konstantina Christina Topka, Babacar Diallo, Diane Samelor, Raphael Laloo, Daniel Sadowski, Cecile Genevois, Thierry Sauvage, Francois Senocq, Hugues Vergnes, Viviane Turq, et al.

▶ **To cite this version:**

Konstantina Christina Topka, Babacar Diallo, Diane Samelor, Raphael Laloo, Daniel Sadowski, et al.. Tunable SiO2 to SiOxCyH films by ozone assisted chemical vapor deposition from tetraethylorthosilicate and hexamethyldisilazane mixtures. Surface and Coatings Technology, 2020, 407, 10.1016/j.surfcoat.2020.126762 . hal-03086943

HAL Id: hal-03086943
https://hal.science/hal-03086943

Submitted on 11 Jan 2021

HAL is a multi-disciplinary open access archive for the deposit and dissemination of scientific research documents, whether they are published or not. The documents may come from teaching and research institutions in France or abroad, or from public or private research centers.

L'archive ouverte pluridisciplinaire **HAL**, est destinée au dépôt et à la diffusion de documents scientifiques de niveau recherche, publiés ou non, émanant des établissements d'enseignement et de recherche français ou étrangers, des laboratoires publics ou privés.

Surface and Coatings Technology, 2021, 407, 126762, doi.org/10.1016/j.surfcoat.2020.126762

Tunable SiO_2 to SiO_xC_yH films by ozone assisted chemical vapor deposition from tetraethylorthosilicate and hexamethyldisilazane mixtures

Konstantina Christina Topka[a,b], Babacar Diallo[c], Diane Samelor[b], Raphael Laloo[b], Daniel Sadowski[b], Cecile Genevois[c], Thierry Sauvage[c], Francois Senocq[b], Hugues Vergnes[a], Viviane Turq[b], Nadia Pellerin[c], Brigitte Caussat[a], Constantin Vahlas[b*]

[a] Laboratoire de Génie Chimique (LGC), Université de Toulouse, CNRS, 4 Allée Emile Monso, Toulouse, 31030, France

[b] Centre Interuniversitaire de Recherche et d'Ingénierie des Matériaux (CIRIMAT), Université de Toulouse, CNRS, 4 Allée Emile Monso, Toulouse, 31030, France

[c] Conditions Extrêmes et Matériaux : Haute Température et Irradiation (CEMHTI), Université d'Orléans, UPR3079 CNRS, 1D avenue de la Recherche Scientifique, 45071, Orléans, Cedex 2, France

*Corresponding author: constantin.vahlas@ensiacet.fr

Postal Address: Centre Interuniversitaire de Recherche et d'Ingénierie des Matériaux (CIRIMAT), Université de Toulouse, CNRS, 4 Allée Emile Monso, Toulouse, 31030, France

Telephone number: +33 534323430,

FAX number: +330534323499

Abstract

Silica and silica-based materials with tunable functionalities are frequently encountered in low-k material applications, porous membranes, and microelectonic devices. In the present study, an innovative O_2/O_3 assisted CVD process for the deposition of such films at moderate temperature is presented, based on a dual precursor chemistry from hexamethyldisilazane (HMDS) and tetraethyl orthosilicate (TEOS). Films with tunable carbon content were obtained through variation of the HMDS flow ratio. A comprehensive FT-IR study reveals the transition of the material from a SiO_xC_yH type film containing -CH_3 moieties, to a methyl-free SiO_x film with the increase of the temperature. At the same time the water contact angle of 81.0° at 400°C is decreased to 52.8° at 550°C, related to the absence of methyl moieties in the latter. Ion beam analysis (IBA) confirms the lack of carbon in the films when deposition temperatures are equal to or exceed 500°C. The resistance to liquid corrosion is investigated as a function of the deposition temperature; SiO_x type films present a low Pliskin etching rate of 15 Å.s^{-1}, with this value increasing to 60 Å.s^{-1} for the SiO_xC_y:CH_3 films produced at the lower temperatures. It is found that the addition of HMDS to a TEOS chemistry can be utilized to modulate the film composition from SiO_x to SiO_xC_yH and by such, tune the film functional properties, in particular its etching rate, opening the way to the development of new sacrificial films.

Keywords: CVD; silica; silicon oxycarbides; Pliskin etching rate; mechanical properties; hydrophilicity

1. Introduction

The production of SiO_2 films through various chemical vapor deposition (CVD) processes has been implemented for a multitude of applications, starting from microelectronics in the nineties [1, 2] to energy harvesting and more recently to environmental protection, waste water treatment and gas separation [3-6]. Silica-based materials such as SiOCH films have also recently attracted attention as gas barriers in food storage, or as gas and water permeation membranes [7, 8]. In contrast to dense films, certain applications such as gas separation require SiO_x selective membranes, with sub-nanometer porosity [9]. Oftentimes, organosilica (SiO_x+R, where R represents methyl, vinyl, phenyl and other hydrocarbon groups) membranes are used to address this need, with the hydrocarbon-content in the films playing an important role in influencing film porosity, and constituting as such a parameter that can be tuned towards desired permeability and selectivity of H_2, He, N_2, CH_4 or SF_3 gases [10].

In other fields such as MEMS applications, certain steps of the fabrication process require sacrificial silica-based layers with high etching rate [11]. Such sacrificial layers are often produced by using **silica from TEOS chemistries** [12], phosphorous doped silica [13], photoresists and other materials, adding multiple steps to the manufacturing process. It has been shown that the etching rate of such SiO_2 films is directly linked to their nanoporosity, their hydration level (Si-OH and Si-H concentrations) and their organic carbon content [14-16]. These characteristics are usually dictated by process parameters, including the adopted chemistry and activation mode of the CVD process. Other applications where organic carbon is required in silica-based films or surfaces relate to the selective Cu or HfO_x CVD deposition through utilization of Si-CH_3-terminated surfaces [17-20].

Carbon and hydrogen loaded silica (organosilica) films with tunable sacrificial behavior are oftentimes produced by plasma enhanced CVD (PECVD) processes that ensure

deposition at low temperature and produce films with good dielectric properties and low mechanical stress [10, 21, 22]. Alternatively, thermal CVD is appealing when potential damage of the substrate material by the directional ionized gases must be avoided, and when deposition of uniform and conformal films on non-line-of-sight patterns and cavities is required. The present work subscribes to the latter frame, since it addresses applications that require deposition of alternating pure SiO_2 and carbonated SiO_x layers, in cavities of thermally sensitive parts. The innovative aspect of the work is the processing of such films from a unique chemistry mixing tetraethyl orthosilicate ($SiC_8H_{20}O_4$, TEOS) with hexamethyldisilazane ($Si_2NC_6H_{19}$, HMDS), two commonly utilized precursors for the deposition of SiO_2 films by CVD [23, 24], and porous, carbonated SiO_x (also designated as SiO_xC_yH) films by PECVD, respectively [25, 26]. Both precursors are in liquid state at room temperature, are non-corrosive and present comparable physicochemical properties; hence, they can be used synergistically to provide films with complementary characteristics. In order to form silica based films at moderate temperature by CVD, HMDS and TEOS require reaction with an external oxidant, such as O_2, $\mathbf{O_3}$ or N_2O [27-30]. In this work, we use an oxygen-ozone mixture, taking advantage of ozone's rapid decomposition, which leads to the production of oxygen radicals that enhance chemical reactivity and enable film formation with elevated deposition rates at low temperatures [31].

The paper is organized as follows: we first present the deposition mechanisms and profiles of films from TEOS-O_2/O_3, followed by those from HMDS-O_2/O_3. Then, we extensively investigate co-deposition from HMDS-TEOS-O_2/O_3 as a function of the deposition temperature, with focus on the additive behavior of HMDS on the produced dual-precursor films in terms of deposition rate, chemical composition, local structure and surface functionality. We extensively analyze the films by FT-IR with the aim to clarify the transition from a sacrificial SiO_xC_y:CH_3 to a more compact SiO_x material, and vice versa. We combine the findings with the elemental composition of the films monitored by Ion Beam Analysis

(IBA), and determine the change in carbon content as a function of the deposition temperature and HMDS flow rate. Then, we reveal and discuss modifications of the functional and mechanical properties of the films, such as wettability and hardness, based on the aforementioned transition from a sacrificial SiO_xC_y:CH_3 to a compact SiO_x material. We apply wet etching corrosion tests to illustrate the increased sacrificial behavior of the carbonated SiO_xC_y:CH_3 films through the addition of HMDS before providing concluding remarks and perspectives for further work.

2. Materials and methods

2.1. Reactor setup

The hot-wall CVD reactor **was** composed of a quartz tube (Ø 46 mm, 700 mm long), heated by a resistive furnace (Trans Temp, Thermcraft Inc.). The setup has been described in our recent work on the modeling of the SiO_2 CVD process from TEOS-O_2/O_3 [32], and was modified minimally by adding an additional bubbler system to house the HMDS (99.9%, Sigma Aldrich) liquid. The modified setup is presented in Fig. S1(a) of *Supplementary Material*. A N_2 (99.9999%, Messer) dilution line heated at 100°C transfer**ed** 1963.5 standard cubic centimeters per minute (sccm) of N_2 , while the N_2 carrier gas line flow**ed** 23.5 sccm through the HMDS bubbler system set to 50 or 62°C, transporting 2.7 or 9.5 sccm of the precursor's vapors in the reactor respectively. This line **was** introduced into the reactor after combining with the dilution line. The flow rates of TEOS (99.999%, Sigma-Aldrich) and O_2 (99.9995%, Messer) **were** 2 sccm and 1960 sccm, respectively. An ozon**izer** (Lab2b Laboratory Ozone Generator, Triogen LTD) connected to the O_2 line **was** operating at its maximum ozone output, supplying the reactor with an O_2/O_3 mixture, at an O_3 concentration of 60 $mg.l^{-1}$ at standard temperature and pressure. The HMDS and TEOS carrier gas lines

were heated downstream of the bubblers at approximately 85°C to avoid recondensation of the precursor vapors.

For all runs with variable temperature, the total gas flow **was** fixed at 4040.7 sccm and the total pressure at 97.3 kPa (730 Torr), monitored with a Pirani (MKS MicroPirani Transducer Series 925C) gauge during vacuum stage preparation and a Baratron (MKS Baratron Type 627) gauge during deposition, downstream of the deposition zone. Five different set point (SP) temperatures, namely 360, 400, 450, 500 and 550°C **were** applied for the deposition of the films, **with the aim to study the transition of the material from SiO_xC_y:CH_3 to SiO_x and its properties along a wide thermal range**. The SP temperatures **were** defined as the temperature measured at 360 mm from the inlet, after which a 140 mm long isothermal region exist**ed**. The samples analyzed in the present work were taken from this isothermal region.

2.2. Film formation on flat substrates

Monocrystalline silicon (100) substrates **were** cut from 280 μm thick wafers (Neyco) into 32×24 mm^2 rectangles. Before being inserted into the reactor, the substrates were degreased as described recently [32]. 18 substrates **were** treated in each experiment, supported vertically by two home-made, stainless steel substrate holders positioned on the row, with a 7 mm deep insertion slot (Fig. S1(b) of *Supplementary Material*). Five runs **were** performed with the HMDS-TEOS-O_2/O_3 chemistry at the previously defined SP temperatures and named hereafter SP360, SP400, SP450, SP500 and SP550. The deposition duration **was** fixed at 30 min for all runs, leading to film thicknesses between approximately 45 and 150 nm in the isothermal zone. For the nanoindentation analysis, additional experiments **were** performed at selected SP temperatures with increased deposition duration, to target higher film thicknesses of at least 500 nm and eliminate substrate interference.

2.3. Measurement of deposition rates and thickness

The average deposition rates **were** calculated from the deposited mass, by measuring each sample's weight gain before and after deposition using a Sartorius Genius Series ME215P analytical balance with 0.015 mg precision. For these results only, we assume**d** uniform deposition on each substrate surface, with an average film density of 2.2 $g.cm^{-3}$. **Naturally, the film composition affects the density of the films, and can thus interfere with the accurate calculation of the deposition rate. For that reason, l**ocal film thicknesses **were cross-checked** by spectroscopic ellipsometry (SE) with a Semilab SE-2000 refractive ellipsometer, operating between 250 nm and 1000 nm wavelength range, at a constant incidence angle of 70°. The measurements **were** performed by probing 3 points along the vertical axis on the surface of each sample. The SE data **were** simulated and fitted in the 250-1000 nm wavelength range using the Semilab SEA software. The calculated results are acquired for a R^2 fit of over 0.99, using a Bruggeman's Effective Medium Approximation (BEMA) model, applying a two-component medium composed of SiO_2 and void. The given thicknesses **were further** confirmed with **the ones** calculated by the Cauchy model, and by observation of transmission electron microscopy (TEM) cross sections for samples SP360 and SP500 (Fig. S2 in *Supplementary Material*).

*2.4. Chemical **bonding state** and composition*

The **chemical bonding state** of the films **was** studied using Fourier transform infrared (FT-IR) spectrometry in transmission mode with a Frontier FTIR MIR/NIR instrument and a custom-made substrate holder that enable**d** the analysis at different angles. The spectra **were** taken by applying a 0° and 60° angle between the sample and the incident beam (Brewster

angle), to clearly observe the TO-LO splitting [33]. The spectral range between 400-4000 cm^{-1} **was** probed with a resolution of 4 cm^{-1}. Sixteen spectrum accumulations **were** taken for each sample, after removal of the background signal. After acquisition, the obtained spectral data **were** further processed by removing the Si substrate's signature and correcting the baseline. Lastly, in order to compare bonding intensities, the absorbance values **were** normalized by each film's thickness, since in FT-IR transmission mode, the intensity of the main SiO_2 absorptions are affected by the thickness of the film [34].

The chemical composition of the films **was** determined by Ion Beam Analysis (IBA) techniques located at the Pelletron facility of CEMHTI in Orléans, France. The contents in silicon, oxygen, carbon and hydrogen **were** determined by Rutherford Backscattering Spectroscopy (RBS), Nuclear Reaction Analysis (NRA) and Elastic Recoil Detection Analysis (ERDA) techniques, on films with thickness in the range of 100-200 nm. RBS and NRA are performed at a 166° detection angle with 2 MeV α particles for the former. Oxygen and carbon concentrations **were** measured through the $^{16}O(d,\alpha_0)^{14}N$ and $^{12}C(d, p_0)^{13}C$ nuclear reactions, using incident deuterons of 0.9 MeV. ERDA measurements **were** performed using a 2.8 MeV alpha beam. The sample **was** positioned at a 15° grazing incidence angle and the recoiled hydrogen atoms **were** collected at a scattering angle of 30°. Ten spectra of 1µC charge **were** successively collected to get enough repeatability and intensity, and achieve a satisfactory signal-to-noise ratio. Due to the presence of a strong desorption of hydrogen for some samples, the ERDA spectra **were** considered individually.

The overall composition of the films **was** obtained by simulating the RBS, NRA and ERDA spectra using the SIMNRA software [35]. $^{16}O(d,\alpha_0)^{14}N$: Sigma Calc-166° (71 mb/sr) and $^{12}C(d,p_0)^{13}C$: Jose 165° (26 mb/sr) cross sections **were** used respectively for oxygen and carbon quantification. Lastly, a polycrystalline silicon wafer with a top layer of 213 nm SiO_2,

an a-Si(H^+) hydrogen standard at $2.19.10^{17}$ H/cm², a carbon and a SiC polycristalline film **were** used for detector energy calibration.

2.5. HRTEM and AFM observations

High-resolution micrographs of the films and corresponding energy dispersive spectroscopy (EDS) elemental information **were** acquired using a JEOL ARM200CF (JEOL Ltd.) TEM instrument operating at 80kV, equipped with double spherical aberration correctors and fitted with a JEOL SDD CENTURIO EDS system. A 0.13 nm probe size **was** used for EDS analysis. Before analysis, the films **were** prepared by Focused Ion Beam (FIB) technique using Ga^+ ions in a FEI HELIOS 600i instrument. Analysis **was** performed immediately after FIB preparation, to minimize contamination of the samples.

The surface roughness of the films **was** measured using an Agilent Technologies 5500 (Fermat) atomic force microscope (AFM) in tapping mode. The tip used **was** an APPNANO ACT model, made of n-type silicon, with a radius of <10 nm. A scan size of 1 µm² **was** used for all measurements.

2.6. Functional and mechanical properties

The hardness and Young's modulus of the films **were** assessed by nanoindentation tests using an UltraNanoIndenter apparatus from CSM Instrument (Anton Paar) equipped with a Berkovich diamond indenter. The applied load **was** gradually increased until a maximum value of 0.5 mN, at which the load is maintained for 30 s. The loading and unloading rate **was** set to 60 $mN.min^{-1}$. Each sample was probed at 5 different locations. Average elastic modulus and hardness **were** calculated from the load vs. depth curves with the method proposed by Oliver & Pharr [36].

Wettability **was** investigated by measuring pure water contact angle with a GBX apparatus using the Young's equation [37], according to which the value of the contact angle depends only on the chemical composition of the material. Water droplets of 0.35 ± 0.01 µl **were** placed carefully onto the sample surface at ambient atmosphere and temperature, and the equilibrium static contact angle was measured at five different locations. The contact angle value **was** assessed by a CCD camera. To obtain the contact angle affected by the surface roughness, the model described by Wenzel [38] **was** applied.

2.7. Wet etching corrosion tests

The corrosion resistance of the films **was** evaluated by applying the P-etch solution test developed by Pliskin [39, 40]. The etching test **was** performed by immersion at 25°C for 30 s under continuous stirring, of a coated sample in a solution of 3 parts hydrofluoric acid (HF, 49 % m.), 2 parts of nitric acid (HNO_3, 70 % m.), and 60 parts of distilled water. The P-etching rate for each sample **was** determined by measuring the thickness of the probed film before and after immersion using ellipsometry, and expressing the total thickness loss in $Å.s^{-1}$ for a given etching time.

3. Results and discussion

3.1. Deposition rates and mechanism

The deposition rate (DR) profiles of films processed from TEOS-O_2/O_3 and HMDS-O_2/O_3 (referred to as TEOS and HMDS hereinafter) are plotted in Fig. 1(a) for SP500 and in Fig. 1(b) for SP550, as a function of the distance from the reactor inlet. Similarly, the DR of films processed from HMDS-TEOS-O_2/O_3 (referred to as HMDS-TEOS hereinafter) at SP500 is presented in Fig. 1(c). The thermal profiles of the corresponding SP temperatures are also

included. For all experiments, the temperature in the first 80 mm of the reactor (pale blue region A) remains low, i.e. between 115 and 170°C. After 80 mm, the temperature increases rapidly (light blue region B) to reach the targeted SP temperature at 360 mm. Lastly, an isothermal zone (blue region C) appears, spanning approximately from 360 to 500 mm. This thermal behavior is representative of all runs.

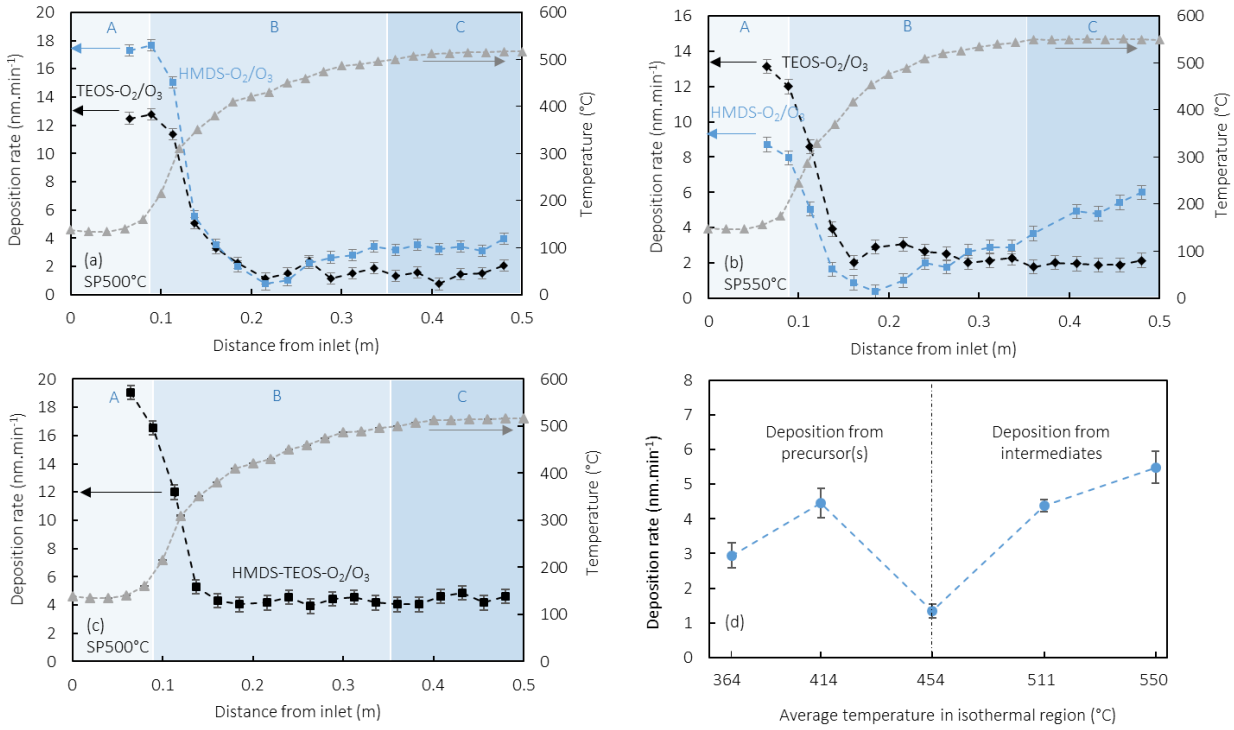


Figure 1. Typical thermal and deposition profiles for HMDS, TEOS, and HMDS-TEOS films. Deposition profiles from TEOS (black diamonds) and HMDS (blue squares) chemistries, at SP500 (a) and SP550 (b). Deposition profile from HMDS-TEOS dual-precursor chemistry at SP500 (c). Blue areas signify the low temperature region at the inlet (A), the gradient temperature region (B) and the isothermal region (C). Corresponding thermal profiles are shown by grey triangles in all three diagrams. (d) Average deposition rates for HMDS-TEOS **films taken from the isothermal region (C) from** runs performed at various SP temperatures.

The presented five deposition profiles show qualitatively similar trends. Relatively high DR values between 12 and 19 $nm.min^{-1}$ are observed at the colder entrance region A, independently from the chemistry used. These enhanced film-formation rates are attributed to the presence of O_3, and to its ability to lead to film formation at low temperatures thanks to its high reactivity through the generation of monoatomic oxygen radicals [31]. **However, films with such high DRs were powdery in nature, delaminating easily from the Si substrate, and were therefore not studied in the present work.** In region B, the DR decreases despite the increase of the temperature, reaching a constant value of around 3 $nm.min^{-1}$ and 2 $nm.min^{-1}$ for HMDS and TEOS processed films respectively in Fig. 1(a), and approximately 4 $nm.min^{-1}$ for the HMDS-TEOS processed films (Fig. 1(c)). **A recent study, dealing with the computational fluid dynamics simulation of the TEOS-O_2/O_3 chemistry, gave access to predictions of the gas phase composition [32]. The simulated model, developed based on literature and experimental data, revealed that the decreasing DR** behavior is due to the rapid consumption of O_3 in region**s** A **and B**, to the benefit of both film formation as well as production of intermediate gas-phase by-products. Due to their similarity in deposition profile, we also argue that film formation by HMDS follows a comparable behavior, reacting with O_3 in region A to produce film and gas-phase species. As such, the quantity of O_3 that is available in the first 5 cm of region B is constantly reducing. For the remainder of region B and then region C, the DR remains low and almost constant, with film formation being possibly dictated by the involvement of silicon-containing intermediate species. These species stem from the decomposition of the precursors after their reaction with O_3, and can lead to film formation once they overcome their respective activation steps. Multiple such intermediates can be produced through gas phase reactions, from both the TEOS [41] and HMDS [28] precursors.

As such, comparison of the DRs from TEOS and HMDS at SP500 (Fig. 1(a)), reveals similar deposition profiles for both chemistries, explained by O_3's diminishing concentration

along the reactor. It is noted that after O_3 consumption, the DR drops to a slightly higher constant value for the HMDS chemistry. Despite the increase of the SP deposition temperature to 550°C (Fig. 1(b)), no notable increase in the DR is observed in the isothermal region (region C) for TEOS. Even though silicon-containing intermediates that are produced from the decomposition of TEOS do contribute to film formation [32], they are, however, consumed in so-called parasitic reactions, such as gas-phase polymerization, **that lead to the transformation of film-forming species into molecules that do not participate in deposition**. **This phenomenon is more pronounced** at elevated temperatures (>450°C). As a result, **the** availa**b**le concentration **of the film-forming species** in the gas phase decreases, which subsequently partially decelerates further increase of silica deposition [27, 42**, 43**].

In the case of HMDS chemistry, a slightly different behavior is observed. Contrary to the TEOS chemistry, HMDS does not result in the stabilization of the DR after the consumption of O_3; instead, it shows a renewed increase. This increase is more noticeable when comparing the two process temperatures: at SP500 (Fig. 1(a)), deposition from HMDS results in a slight increase of the DR after 0.2 m and reaches a value of approximately 3**.4±0.3** nm.min^{-1} in the isothermal region C, while at SP550 (Fig. 1(b)) the increase is more pronounced and DR values in this region exceed 4 nm.min^{-1}**, averaging at 4.9±0.8 nm.min^{-1}**. This could be explained by the fact that the intermediates coming from HMDS' decomposition are not participating in parasitic gas-phase reactions. As a result, they could actively contribute to film formation, and overcome their activation step once the reactor temperature exceeds approximately 500°C.

It is noted that the precursor flow rates used were the same (2.7 sccm for HMDS and 2 sccm for TEOS), whether they were tested separately or together in the utilized chemistries. Logically, the dual precursor system HMDS-TEOS has a deposition behavior that is dictated by the participation of both precursors to the film formation. Hence, at SP500 (Fig. 1(c)) the

DR is stabilized after the consumption of O_3, however, at a value higher than that of the separately TEOS and HMDS chemistries.

The DR of the HMDS-TEOS chemistry, averaged across the six samples located in the isothermal region (region C) is shown in Fig. 1(d), as a function of the SP temperature. It presents a wavy behavior between 1 and 6 nm.min^{-1}. More specifically, the DR increases from SP360 to SP400, then decreases at SP450, after which it increases again from SP450 to SP550. This non-monotonous trend has also been observed for the thermal CVD of SiO_2 from TEOS [43], and is explained through the participation of distinct reactive species in SiO_2 film formation, depending on the temperature. For temperatures lower than 400°C, deposition depends primarily on the precursor molecule and on the presence of O_3 in the gas phase. At higher temperatures, the precursor molecules decompose into Si-containing gaseous intermediate species. As a result, the deposition mechanism switches to an intermediates-centered mechanism. Moreover, parasitic gas phase reactions that consume film-forming species are activated in the high-temperature regime, resulting in the decrease of the DR.

As was previously pointed out, an upwards slope is observed in region (C) for the HMDS chemistry at SP550 (Fig. 1(b)), while the DR from TEOS remains constant. It is therefore assumed that when utilizing the dual precursor HMDS-TEOS chemistry, any increase in the DR above 500°C is primarily due to the addition of HMDS. The dip at SP450 in Fig. 1(d) could be related to an overall transition of the deposition mechanism from precursor-governed to intermediates-governed mechanism, lowering as a result the DR. Potentially, a high contribution of carbon rich species to deposition could also be involved in this behavior, as will be shown in later sections. The deposition rate profiles for all experimental runs using the HMDS-TEOS chemistry are available in Fig. S3 of *Supplementary Material*.

3.2. Film surface morphology

AFM surface micrographs for HMDS-TEOS films deposited at all five SP temperatures are presented in Fig. 2(a) to (e). The micrographs at the lower three SP temperatures reveal rough surfaces, in contrast to the two higher temperatures SP500 and SP550, which present a generally smoother surface. This trend is also confirmed when plotting the root mean square (RMS) roughness as a function of the SP temperature as shown in Fig. 2(f). The RMS of surfaces prepared at SP360, SP400 and SP450 is spanning between 3 and 4.5 nm, whereas it decreases to values around 0.5 nm for SP500 and SP550. SEM surface micrographs, representative of the two observed surface morphologies, are also reported in Fig. 2(g) and (h), corresponding to samples processed at SP360 and SP500, respectively. In agreement with the AFM observations, the films' morphology appears rough at lower SP temperature, becoming smoother when the latter is increased to SP550. Additionally, they reveal a difference in the growth and nucleation mechanisms: an apparent 3D-dominated nucleation and growth behavior is observed at lower temperatures, attributed to the high DR combined with the limited mobility of the adsorbed species. At elevated temperatures, the species participating in film formation have higher surface mobility, due to the increased energy available through the increase of the process temperature. As such, they are able to diffuse more easily on the surface, following primarily 2D growth behavior, and lead to the production of denser and smoother films.

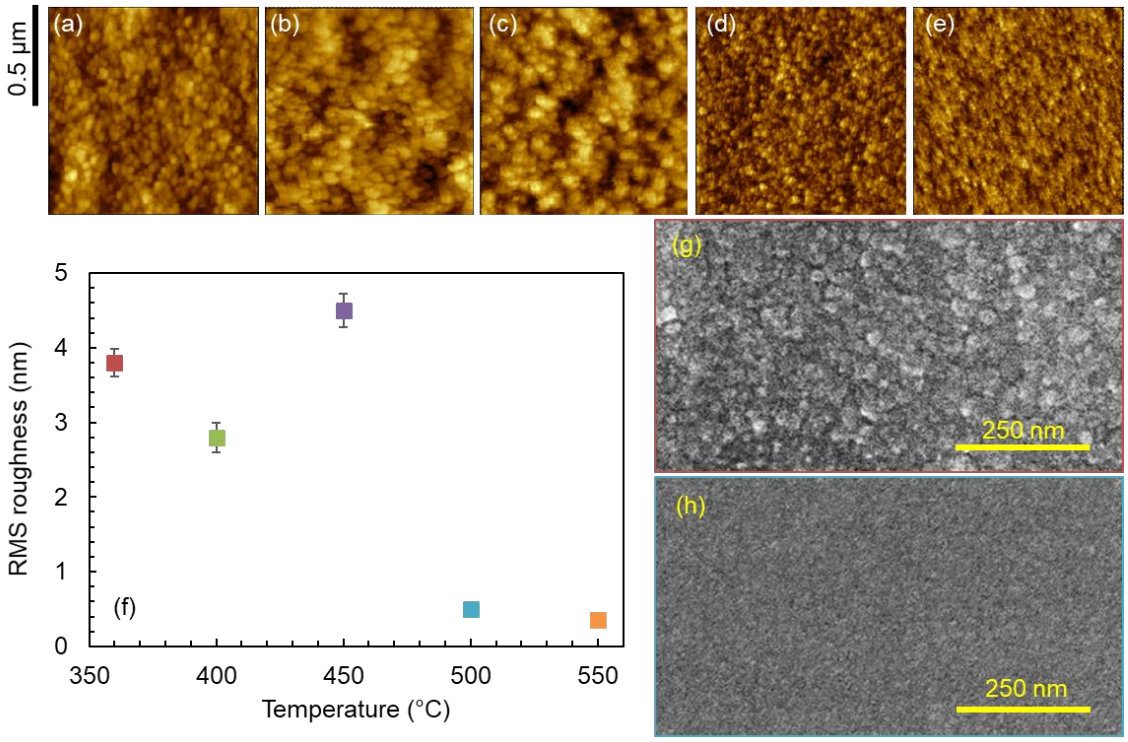


Figure 2. Surface topography and roughness of HMDS-TEOS films at various SP temperatures. AFM 1µm^2 surface topography at SP360 (a), SP400 (b), SP450 (c), SP500 (d) and SP550 (e). RMS roughness of HMDS-TEOS films for different temperatures measured by AFM **(f)**. Inset images show SEM surface morphology for SP360 **(g)** and SP500 **(h)**.

Overall, the surface roughness decreases with increasing temperature, with the exception of SP450. According to Gil et al. [44], who performed PECVD of silicon oxide films from HMDS and O_2, the organic carbon content, incorporated in the films as CH_3 moieties, influences the surface roughness. The authors reported that increasing oxygen flow aids in the decomposition and oxidation of HMDS, which leads to a decrease in the amount of Si–$(CH_3)_x$ bonds in the films, and subsequently to the decrease of surface roughness. In our work however, the O_2/O_3 flow rate remains unchanged across all runs, with the temperature being the only variable. Based on their findings though, we argue that the increased roughness observed at SP450 could be a result of the transitioning deposition mechanism happening at this temperature, and propose that this transition introduces more CH_3 moieties in the films,

increasing in turn the RMS roughness. According to the above, we also propose that the surface roughness can be adjusted by tuning the CH_3 content of the films through variation of the HMDS:TEOS, or (HMDS+TEOS):O_2/O_3 ratio, in combination with the deposition temperature.

*3.3. Film **chemical bonding state***

The infrared spectrum of a HMDS-TEOS film produced in the isothermal region of SP360 is presented in Fig. 3, as representative of the samples processed at low SP temperatures. A survey spectrum of a HMDS-TEOS film deposited at SP500 is presented for comparison in Fig. S4 of *Supplementary Material*. Both of these acquisitions were done at a Brewster incidence angle of 60°, with the aim to increase the signal-to-noise ratio and to reveal additional information related to the silica network [33].

We first identify and discuss the main peaks of the survey spectrum in Fig. 3, and present the evolution of the various moieties as a function of the SP temperature in respective inset graphs. Globally, the films are characterized as a silica-based material, evidenced by the strong absorption at 1064 cm^{-1} attributed to the Si–O–Si transverse optical asymmetric stretching mode (TO3) [10, 45]. This absorption is characteristically present in SiO_x films prepared by TEOS-O_2/O_3 and HMDS-O_2 thermal CVD [30]. Other absorptions related to the Si–O–Si network are found at 448 cm^{-1} and 806 cm^{-1} corresponding to its transverse optical rocking (TO1) and bending **or stretching** (TO2) modes, respectively [45]. A fourth transverse optical absorption (TO4) can be observed at lower incidence angles (0°), appearing as a shoulder between 1100 cm^{-1} and 1250 cm^{-1}, and has been attributed to various phenomena, among which strains in the network [46] or out of phase vibrations of the TO3 mode [47, 48]. However, when inspecting the spectrum at a 60° angle, the TO4 peak, as well as its LO4 pair, are obscured under the split of the main Si–O–Si asymmetric stretching absorption into the

transverse (TO3) and longitudinal (LO3) optical components at approximately 1064 cm^{-1} and 1216 cm^{-1} [33].

The presence of carbon is also identified in the films, mostly in the form of hydrocarbons. Methyl-related absorptions are observed at different wavenumbers as indicated in Fig. 3. Generally, weak absorptions within the 2800-3000 cm^{-1} range are related to stretching vibrations of the saturated C–H bonds [25, 49] with the increase in their intensity corresponding to an organo-rich structure [50]. In the present work, one such absorption is found at 2970 cm^{-1} and is assigned to the CH_3 asymmetric stretching of CH_3 functional groups [28]. Secondly, the absorption at 1278 cm^{-1} is related to the symmetric CH_3 bending vibrations of Si-$(CH_3)_x$ groups [44, 51], while the shoulder at 845 cm^{-1} is attributed to the rocking CH_3 vibration in Si–$(CH_3)_3$ groups [28, 52]. The evolutions of these three absorptions are plotted versus the deposition temperature in the inset figures Fig. 3(a), (b) and (c). This information reveals that the CH_3 related absorptions follow a similar behavior, and their intensities decrease at higher temperatures, with all three methyl absorptions reaching zero for temperatures equal to or higher than 500°C. This indicates that films deposited above 500°C do not contain carbon, thanks to the additional provided energy being high enough to break the Si-CH_3 bond in the starting molecule (HMDS in the present work). A spike is observed though for films processed at 450°C. We propose this increase in methyl moieties to be linked to the transition in the deposition mechanism at this specific temperature as discussed in section 3.1. Additionally, the probing of an increased methyl concentration in films deposited at SP450 correlates well with the RMS roughness results discussed in section 3.2, and demonstrates how a higher methyl content increases the surface roughness. In the histogram of Fig. 3(d), the three methyl absorptions are probed for films processed under two different HMDS flow rates, with the temperature constant at 400°C. Higher concentrations for all three CH_3 modes are found at the higher HMDS flow rate. This, combined with the fact that no methyl incorporation was observed on TEOS films (to be published), indicate that the methyl

moieties originate from the HMDS molecule, as was also observed by Gil et al. [44] and Lee et al. [53]. This subsequently impacts film surface roughness, suggesting that coatings with tunable properties can be produced based on selected variations of the two precursors' flow rates.

Other vibrations related to carbon are observed at 1620 cm^{-1} and 790–820 cm^{-1}, corresponding to olefinic carbon [54], and Si–C stretching bonds respectively [49]. However, the absorption at 1620 cm^{-1} can also be related to weakly adsorbed molecular water, that can be removed by heating [55, 56]. The evolution of the 1620 cm^{-1} absorption versus the temperature is presented in Fig. 3(f), and we note that it follows neither the intensity evolution nor the characteristic spike at 450°C coherent for the methyl absorptions discussed above. This makes us more inclined to attribute this peak to adsorbed molecular H_2O instead of a carbon-related absorption.

Further indications of carbon in the films are observed through a rocking vibration of CH_3 from $Si(CH_3)_2$ groups, found at 800 cm^{-1} [52]. Additionally, a small absorption is found at 1410 cm^{-1} corresponding to the asymmetric CH_3 bending vibrations in Si-$(CH_3)_x$ [51], while a weak absorption at 1478 cm^{-1} could originate from the bending vibration of methylene (CH_2) groups [10]. Further absorptions related to CH_2 vibrational modes can be observed at 1372 cm^{-1}, **potentially** related to scissoring and wagging CH_2 vibrations in Si–CH_2–Si bondings [**10**, 53, 57]. The signal for Si–CH_2–Si, normally found at 1350 cm^{-1}, is usually weak [10] and was not observed in the present work. At the same time, a related absorption, namely the wagging vibrations of CH_2 in Si-CH_2-Si, can be typically found at around 1060 cm^{-1} [53], but is most likely overshadowed by the strong Si–O–Si asymmetric stretching absorption at 1064 cm^{-1}. Similarly, the main peaks related to Si–O–C and Si–CH_2–Si, normally reported at 1100 cm^{-1} and 1000 cm^{-1} [58, 59], possibly overlap once again with the strong Si–O–Si network absorptions. As such, their presence cannot be confirmed with certainty.

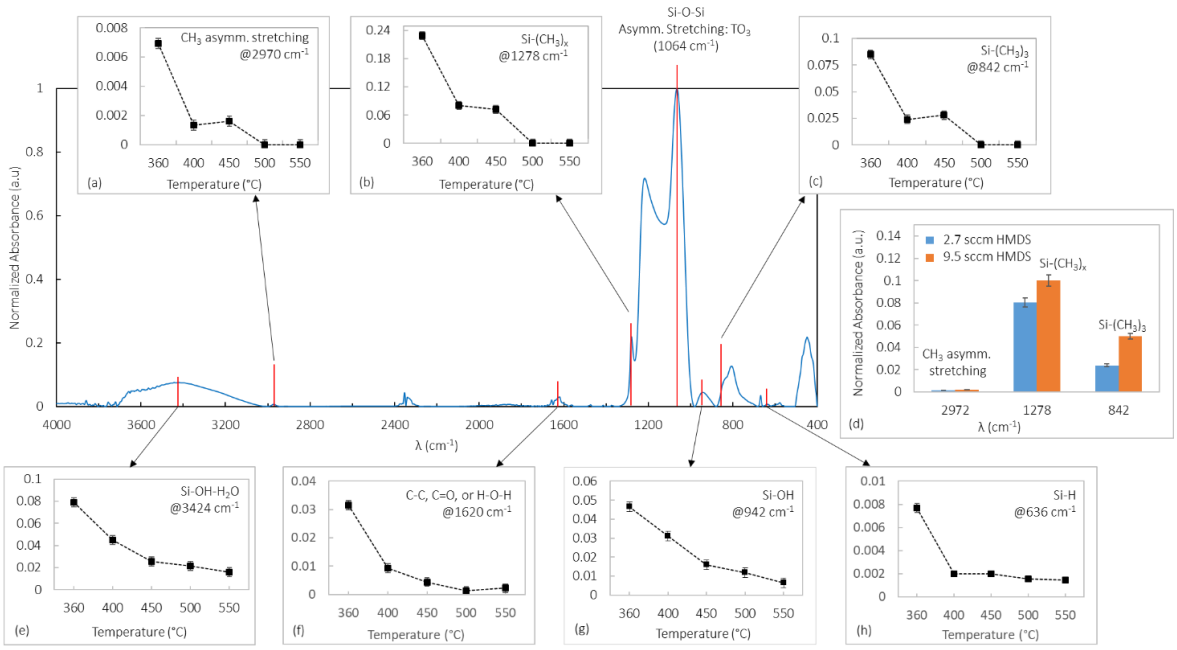


Figure 3. FTIR survey spectrum of a HMDS-TEOS film deposited at 360°C, analyzed for an incidence angle of 60°. Inset diagrams show the intensity's evolution of the CH_3 asymmetric stretching (a), the CH_3 symmetric bending in Si-$(CH_3)_x$ (b) and rocking CH_3 vibration in Si–$(CH_3)_3$ (c) as a function of the SP temperatures. Inset histogram (d) shows these three absorptions for two different HMDS flow rates, at SP400. The remaining inset figures show the evolution of water-bonded silanol (e), water (f), free Si-OH (g) and Si-H (h) absorptions with the SP temperature.

Further inspecting Fig. 3, the large band between 3000 and 3700 cm^{-1} is noted, which contains absorptions related to water and Si-OH bonds, and hints to a hydrated network. It is known that Si-OH terminated silica films readily absorb water after exposure to air [60]. As such, Si-OH bonded with water is probed at ~3400 cm^{-1} [42], while free –OH silanol groups are probed at ~3650 cm^{-1} [42, 61]. An additional silanol fingerprint is found at 942 cm^{-1} [30, 44]. The intensity of both water-bonded and free Si-OH groups is tracked as a function of the SP temperature in Fig. 3(e) and (g), revealing a decreasing absorption for films deposited at higher temperatures. This behavior suggests that the concentration of silanol bonds decreases

when the temperature increases, with the silicon-hydroxyl bond being broken to lead to new Si-O-Si and a less hydrated network.

It is worth noting that no SiH_2 absorption, normally appearing in the range 1900-2200cm^{-1} is observed in any of the spectra [62, 63]. A weak absorption appears at 2353 cm^{-1}, which could correspond to a Si-H stretching mode [30]. However, atmospheric CO_2 is probed at 2353 cm^{-1} as well [64, 65], originating from incomplete background signal removal and as such, absorption at this wavenumber cannot be entirely assigned to Si-H. The weak absorption observed at 636 cm^{-1} could relate to the Si-H bending absorption normally found at 630 cm^{-1} [66] or Si-H wagging/rocking at ~640 cm^{-1} [62]. However, when its intensity is traced as a function of the SP temperature (Fig. 3(h)), it is shown that the minimal Si-H absorption falls to insignificantly low values for $T \geq 400°C$. In light of the above, we assume that films processed from HMDS-TEOS are devoid of Si-H bonds.

3.4. Evolution of silica network

A zoom in the 1300-950 cm^{-1} region of the FT-IR spectra is presented in Fig. 4, showing two SiO_2 vibrational modes (TO3 and TO4) and a methyl one (CH_3 symmetric bending in Si-$(CH_3)_x$ groups) for all SP temperatures. The evolution the two silica vibrational modes, such as the shift of their position or their broadening, reveals information regarding the porosity [67], level of disorganization and strain [68] and the presence of defects or impurities in the silica network, and will be discussed in detail in the present section.

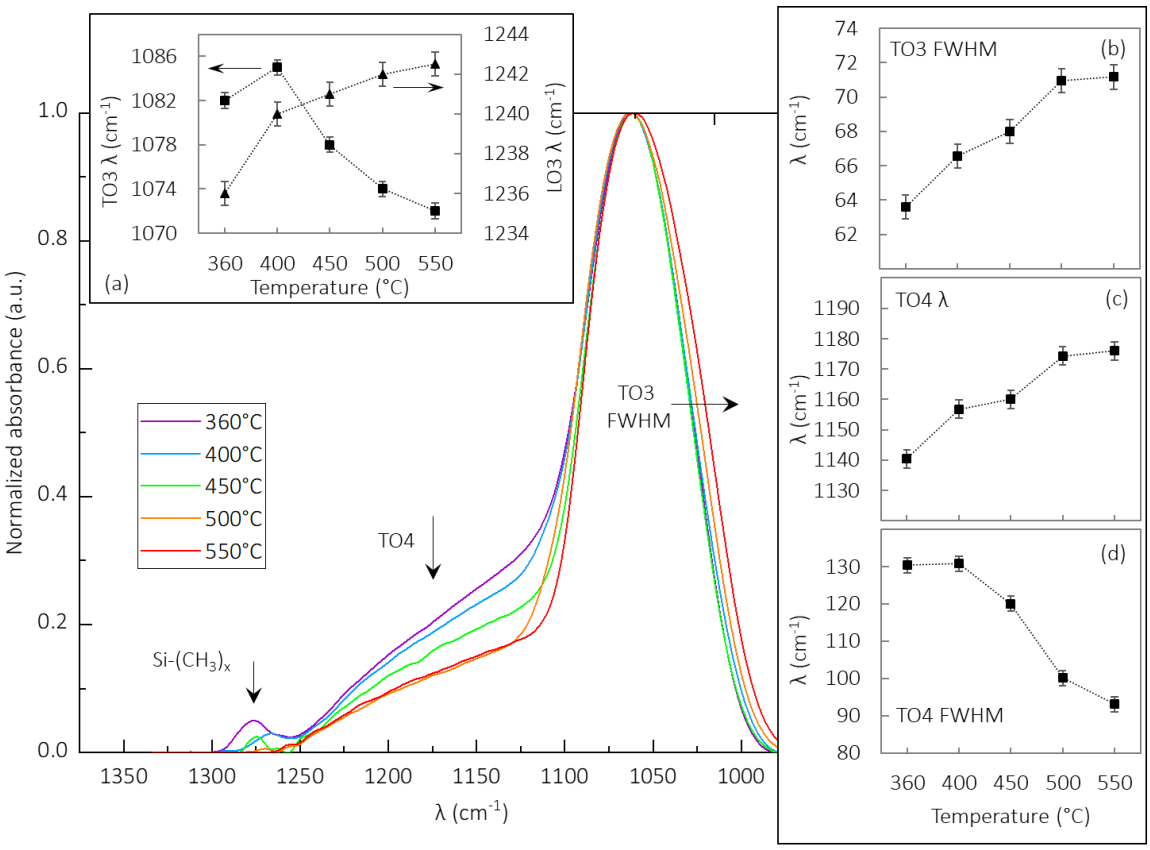


Figure 4. Evolution of the FT-IR spectrum of HMDS-TEOS films deposited at various SP temperatures, analyzed for an incidence angle of 0°. Inset diagram (a) shows the evolution of the TO3 and LO3 components, as observed for an incidence angle of 60°. Right hand-side inset diagrams show 0° angle evolution of the TO3 full width half maximum (b), the TO4 position (c), and the TO4 full width half maximum (d) as a function of the SP temperature.

First, the position of the TO3 asymmetric Si-O-Si stretching vibration is noted. Even though a change in its wavenumber is not visible for 0°, observation is facilitated when it is inspected under an incidence angle of 60°, which enhances interaction between the electromagnetic field and the film. At this oblique angle, the LO3 and TO3 components are separated [33] and can be studied as a function of the temperature, an evolution that is traced in Fig. 4(a). It is revealed that an increase in SP temperature results in a shift of the TO3 mode towards lower wavenumbers, and in a shift of the LO3 towards higher ones. According to Ponton et al. [14], a shift of the TO3 peak towards lower wavenumbers is a trend commonly

observed in silica films processed at temperatures up to 600°C [67, 69]. At temperatures higher than 600°C, a TO3 shift towards lower spatial frequencies hints at a decrease in film density; however, this is not the case for films deposited below 600°C. As argued by Ponton et al., the shift of the TO3 peak towards lower wavenumber is a behavior influence by multiple parameters such as film impurities, defects, or mechanical strain and thus no clear correlation to the network densification can be derived for films deposited below 600°C. In contrast, the LO3 component is less biased by other types of vibrations [33] and its shift towards higher wavenumbers can be correlated more safely with a densification of the SiO_2 network as the process temperature is increased.

Additionally, the TO3 peak broadens as shown in Fig. 4, an evolution observed more closely in the inset Fig. 4(b). As indicated, the TO3 absorption becomes broader with increasing temperature, normally hinting at a disorganization of the network [50]. However, instead of being solely related to the full width at half maximum (FWHM), the broadening is impacted by a change in the shape of the TO3 peak. More specifically, when probed for high temperatures, the TO3 peak deviates from a gaussian or lorentzian function, its shape becoming asymmetric and increasing on one side, suggesting the contribution of additional absorptions [70].

Regarding the asymmetric stretching “out of plane” mode TO4 shoulder, a decrease in its intensity is observed with the temperature, while its position shifts towards higher wavenumbers, a trend more closely presented in the inset Fig. 4(c). Interestingly, the increase in TO4 position follows a similar trend to the broadening of the TO3 vibrational mode, indicating the parallel and linked evolution of these two absorptions. Generally, the TO4 shoulder is associated with Si-O-Si groups that are impacted by porosities [46], or impurities related to hydrogen species such as water or silanol [69]. Moreoever, Si-O-Si groups vibrating at the TO4 frequency also indicate at structural disorder of the SiO_4 tetrahedra [53]. As a result, the decrease in TO4 intensity with the temperature translates into more organized

tetrahedra, and is coherent with the lower signature of hydrogen species (H_2O, Si-OH, and hydrocarbons) observed at higher temperatures, as was presented in section 3.3. The shrinking of the TO4 shoulder is also noted, its evolution presented in the inset Fig. 4(d). The decrease in TO4 FWHM is readily associated with the further organization of the network [68], and in good correlation with the results discussed so far.

3.5. Chemical composition by IBA techniques

Three IBA techniques, namely RBS, NRA and ERDA were used to determine the elemental composition of the HMDS-TEOS films. The atomic concentrations of Si, O, C and H are represented in Fig. 5 as a function of the SP temperature. **No nitrogen was detected in any of the produced films.** The concentration of carbon reaches approximately 5 at.%, and is found in films deposited at 360, 400 and 450. No carbon is detected for films deposited at 500 and 550. Globally, the carbon concentration tends to decrease with the deposition temperature, although a slight spike is observed at 450°C. It is recalled that a similar spike was noted in the intensity of the -CH_3 asymmetric stretching, symmetric bending and symmetric rocking absorptions (Fig. 3(a) to (c)) at 450, while at 500 and 550 their intensities dropped to zero. This reveals a good match between FT-IR and IBA results.

Based on the compositional analysis and the infrared absorptions detailed in Fig. 3, two different materials are identified hereinafter. The one material type is given a generic formula SiO_xC_y:CH_3, with carbon encountered as Si-C, but most predominantly in the form of methyl moieties. This type of material is assigned to films processed at temperatures equal or lower than 450°C depicted by the grey area in Fig. 5. The other type of material is defined as a carbon-free, sub-stoicheiometric silicon oxide, SiO_x (off-white area in Fig. 5) and is encountered for films deposited at 500 and 550°C. The stability domains of the two materials

also coincide with the reported morphological evolution probed by AFM, namely rough and smooth surfaces for the SiO_xC_y:CH_3 and SiO_x surfaces, respectively.

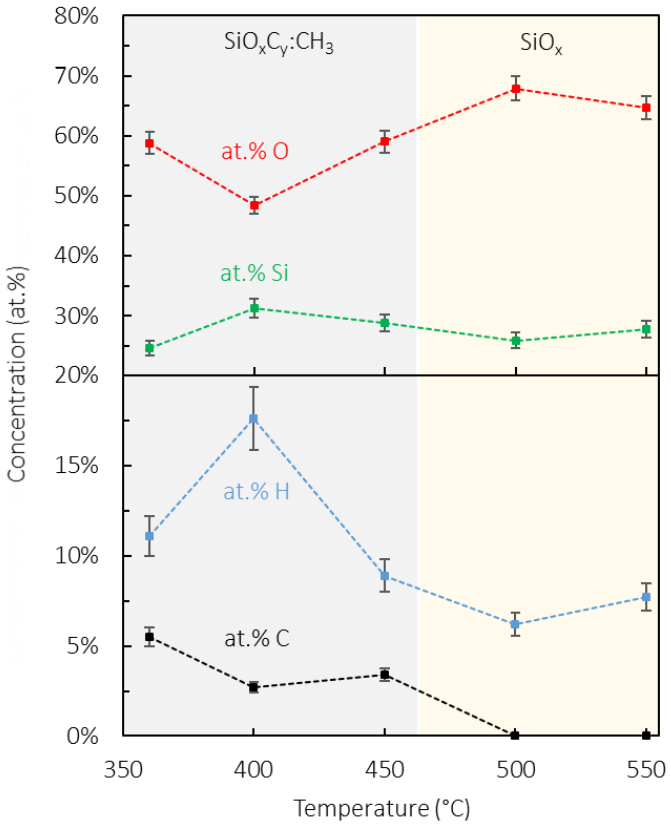


Figure 5. Evolution of HMDS-TEOS films composition as a function of SP temperature, obtained from the first spectral acquisition through IBA techniques. Grey and off-white areas signify SiO_xC_y:CH_3 and SiO_x material domains respectively.

Regarding the hydrogen content in the films, it should be noted that the evolution of its atomic concentration does not follow, in shape, that of the carbon. This behavior is expected, when taking into consideration that hydrogen is not present only in CH_3 moieties, but is also involved in H_2O and Si-OH hydrated species, as revealed by the FT-IR spectra. The hydrogen content measured for SiO_xC_y:CH_3 films is high, with values between 8 and 17 at.%, depending on the process conditions, and decreases to around 7 at.% for SiO_x type films. An opposite evolution is observed for oxygen. The measured oxygen content is higher for SiO_x

compared to SiO_xC_y:CH_3 films. The determined silicon content remains almost constant, with a slight minimum atomic concentration observed at the lowest SP temperature of 360 °C, for which the carbon content is the highest measured.

3.6. Hydrogen desorption

The evolution of the ERDA probed hydrogen content during ten sequential acquisitions is presented in Fig. 6 for a sample processed at SP400. The value of 120.10^{15} at.cm^{-2} obtained during the first acquisition corresponds to 17 at.% H concentration in the film, reported in Fig. 5. A decrease of the hydrogen content is observed in the first three spectral acquisitions down to a value of ca. 35.10^{15} at.cm^{-2}, after which the measured hydrogen concentration appears constant. This phenomenon was observed in samples produced at all SP temperatures, and corresponds to the desorption of a significant amount of hydrogen atoms during the interaction of the film with the 2.8 MeV ion beam. The desorption percentage, as calculated from the difference between the first and the third acquisition, is presented in the inset graph of Fig. 6, and its evolution is tracked for all temperatures studied. It appears that the SiO_xC_y:CH_3 type films show a stronger desorption behavior, while the SiO_x films are less affected by this phenomenon, since the desorption of hydrogen atoms between the first and the third acquisition drops from ca. 60 % down to 20 % when crossing the stability domains of the two kinds of ceramic films. This desorption behavior is attributed to the high hydrogen concentration in the SiO_xC_y:CH_3 films as measured by ERDA, additionally established from the strong intensity of hydrogen-involving bonds shown through FT-IR analysis. Indeed, the highest hydrogen desorption is observed for the SP400 films (inset Fig. 6), which also have the highest hydrogen atomic concentration (Fig. 5).

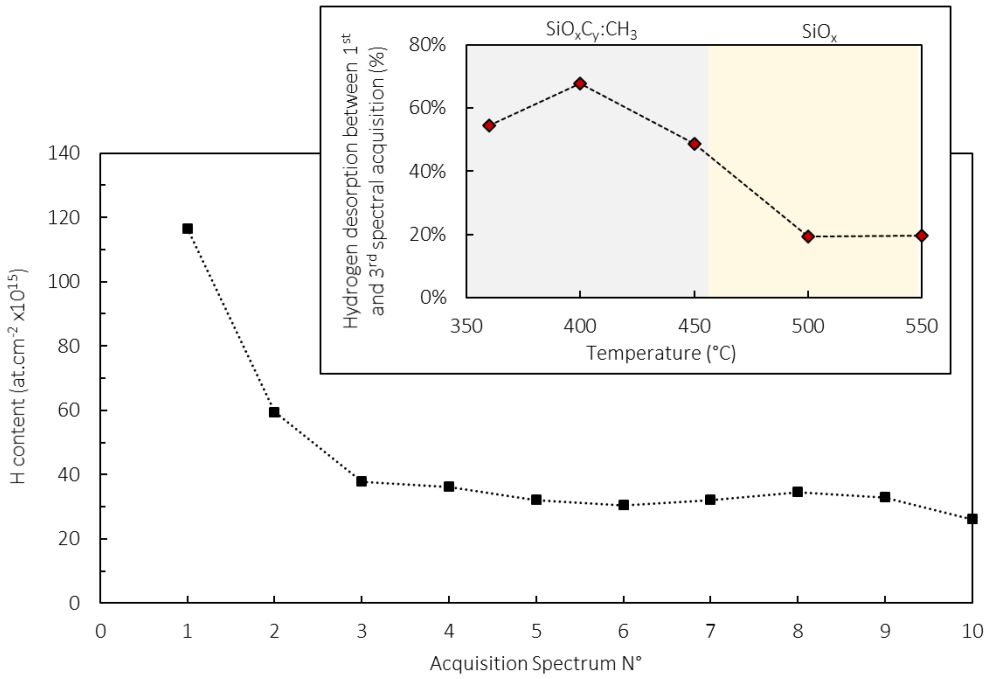


Figure 6. Hydrogen content of an SP400 HMDS-TEOS film as analyzed by 10 consecutive ERDA spectra acquisitions. Inset figure shows evolution of the percentage of hydrogen desorption between the first and third spectral acquisitions as a function of the SP temperature.

3.7. Film morphology

TEM cross sectional micrographs for a HMDS-TEOS film deposited at 360°C are shown in Fig. 7. The TEM micrograph shows that the film is homogeneously deposited on the Si substrate at this scale, with an average thickness of 66±2 nm. Its top surface in contact with the FIB carbon layer is relatively rough, in agreement with the 3.8 nm RMS roughness determined by AFM. High resolution TEM shows intimate contact with no interfacial porosity between the film and the Si substrate. The SiO_xC_y:CH_3 film is amorphous, as shown by Fast Fourier Transform imaging. The EDS profile performed from the Si substrate to the film surface, yields 5.5, 35.0 and 59.5 at% C, Si and O concentration, respectively, which

favorably compares with the IBA results for this film (6.2, 27.9, 65.9 at.% for C, Si and O considering H-free films).

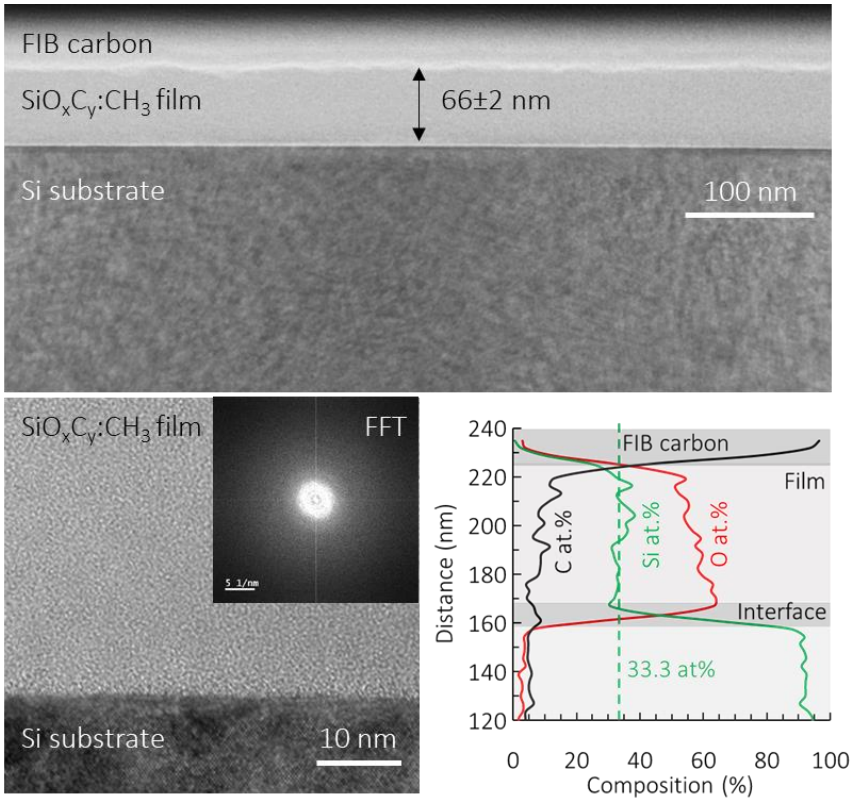


Figure 7. TEM analysis of a HMDS-TEOS SP360 film. Cross section (top), high-resolution cross section and Fast Fourier Transform (bottom left), and EDS elemental profile (bottom right).

3.8. Wettability

The water wettability of the HMDS-TEOS films was assessed and the measured contact angles are presented in Fig. 8 as a function of the deposition temperature.

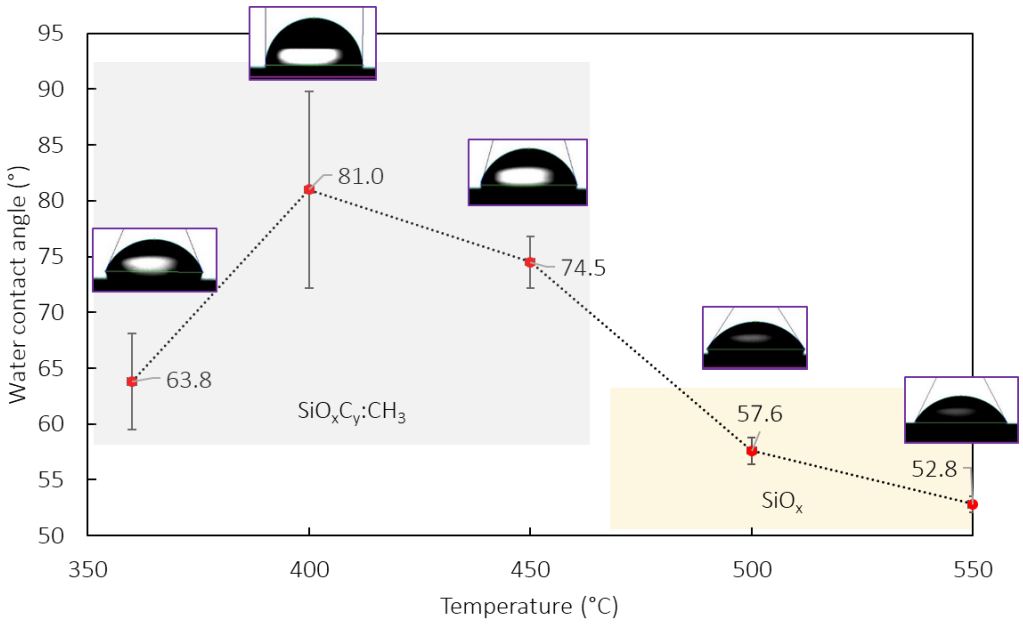


Figure 8. Water contact angles for HMDS-TEOS films and their evolutions as a function of the SP temperature. Grey and off-white regions signify SiO_xC_y:CH_3 and SiO_x material domains respectively.

Overall, the films are hydrophilic; however, there are noticeable differences among them, depending on the deposition temperature. The hydrophilic character of the high SP temperature films is rather strong, with a 57.6° contact angle for SP500, and an even lower contact angle of 52.8 for SP550. In contrast, a decrease of the deposition temperature results in a noticeable increase of the contact angle, which passes from 57.6° to 74.5° between the SP500 and SP450 films. This increase is maintained upon further decrease of the deposition temperature, with the contact angle for the SP400 film being 81.0°, i.e. the highest value noted among the produced films. The trend is inverse for the SP360 film, for which the contact angle decreases to 63.8°. This behavior reveals a clear distinction among the films, namely between the carbon-free material domain defined as SiO_x at high temperature, and the carbon-rich SiO_xC_y:CH_3, processed at the lower SP temperatures. The reduced hydrophilic character of the latter, despite the increase in roughness that should normally enhance the

hydrophilicity according to Wenzel [71], is attributed to the presence of carbon in the form of methyl moieties, as was observed by infrared spectroscopy (Fig. 3). According to Gil et al. [44], the methyl-termination of surfaces increases the contact angle, and renders the films less hydrophilic. Additionally, HMDS is widely used for as a silylation agent in hydrophobic coatings, removing Si-OH surface termination and replacing the silanol species by Si-CH_3 ones, to increase film hydrophobicity [72, 73]. Indeed, the intensity of all methyl-containing bonds in Fig. 3(a) to (c) is higher at low deposition temperatures, globally explaining satisfactorily the less hydrophilic character of SiO_xC_y:CH_3 films.

Nonetheless, the above cannot explain the behavior of the SP360 sample, for which the contact angle is lower than that of SP400. A possible explanation for this behavior comes from the synergistic decrease of the hydrogen and the increase of the oxygen contents between SP400 and SP360 films, which could correspond to increased network hydration at the lowest deposition temperature, as shown by the evolution of the vibration at 3424 cm^{-1} in the FT-IR spectra (Fig. 3). At this point, the results of Wei et al. can be considered [74], who deposited films by HMDS via PECVD at low temperatures. Their HMDS films gave a contact angle of 87-90°, but this value decreased to <10° when O_2 plasma was utilized. The authors proposed that this change of wettability stems from the significant surface chemistry variation caused by the change in reactants used, specifically the addition of oxygen (which reduces –CH_3 incorporation). In the present work, it is evident that wettability does not only depend on film surface methylation, but is a parameter affected by the synergy between global surface chemistry (-CH_3, -OH, water, etc.), roughness, and surface energy.

3.9. Wet etching corrosion resistance and Hardness

The wet etching corrosion resistance (Pliskin test) and the hardness of the films are presented in Fig. 9 as a function of the deposition temperature.

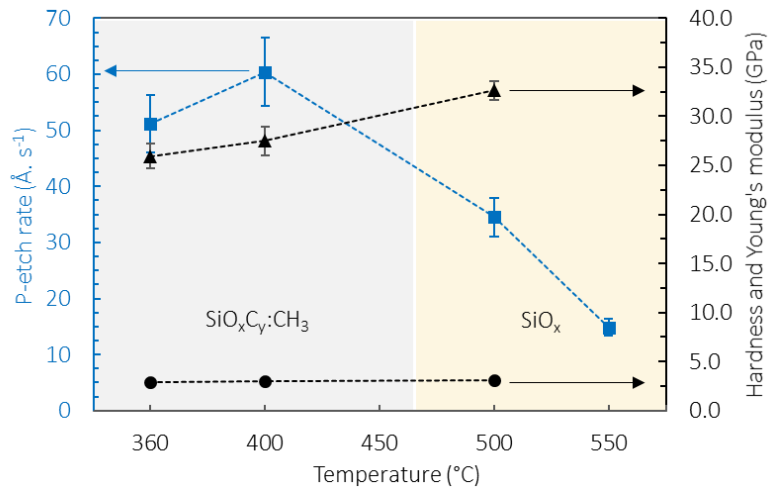


Fig. 9. Performance of HMDS-TEOS films in terms of corrosion resistance and mechanical properties. Evolution of Pliskin-test wet etching rates (squares), Young's modulus (**triangles**) and hardness values (**circles**) from nanoindentation analysis, plotted versus various SP temperatures. Grey and off-white regions signify SiO_xC_y:CH_3 and SiO_x material domains respectively.

As can be observed in Fig. 9, the etching rate of HMDS-TEOS films at low SP temperatures is between 50 and 60 Å.s^{-1}, dropping down to 15 Å.s^{-1} at SP550. It is evident that the etching rate depends strongly on the process temperature, and is decreasing for higher SP temperatures. This behavior is linked to the composition and intrinsic nature of the material, with the SiO_xC_y:CH_3 films exhibiting lower wet etching corrosion resistance compared to the SiO_x ones. Decreasing trends for the etching rate with increasing temperature for films by HMDS and O_2 , **O_3** or N_2O are also observed in the literature [29], linking the change in etching rate to an effect of the composition.

To further consolidate this claim of composition-effect, the FT-IR results of Fig. 3 suggestd that the lower H_2O incorporation and the elimination of CH_3 at higher SP temperatures is one of the reasons for the improvement in corrosion resistance. Additionally, the breakage of Si-OH bonds when depositing at higher temperatures also contributes to the

formation of new Si-O-Si bonds and increases network crosslinking [30]. Additionally, consideration of the IBA results (Fig. 5) reveals that the P-etching rate follows the overall trend of the atomic hydrogen content. This information is coherent with the etching mechanism of HF solutions, under which the silica network is dissolved primarily through a dissolution reaction initiated via the substitution of surface silanol groups (-Si-OH) by -Si-F groups [75].

It is noted though that a high corrosion resistance is not always the target. On the contrary, in applications requiring sacrificial films, such as those encountered during the manufacturing process of MEMS devices, the opposite behavior is desired, and etching rates should be as high as possible to decrease the releasing time of the manufactured components [13]. In such cases, the interest is shifted towards materials with higher porosity, a property which, in the case of HMDS-TEOS co-deposition, can be tuned through adjustment of the HMDS flow rate, the ratio between the two precursors and the oxidant, and even the deposition temperature. Therefore, optimization of the deposition conditions can lead to the production of a material with desired nanoporosity aand etching rate, able to meet the requirements of the target-application.

The elastic modulus and hardness of HMDS-TEOS films are also presented in Fig. 9. Elastic modulus increased with the temperature from 25.9±1.3 to 32.6±1.0 GPa, a change which is linked mostly to the transition of the material's nature from SiO_xC_y:CH_3 to SiO_x, and the increase in Si-O-Si bonds in the film [76]. Hardness is measuring 2.9±0.19 GPa at SP360, and increases slightly to 3.1±0.15 GPa at SP500. Despite the transition of the material type from SiO_xC_y:CH_3 to SiO_x, the films present an almost constant hardness of approximately 3.0±0.17 GPa, independent from the process temperature. Such a behavior has also been reported by Merekov et al. [77] , who performed Laser-assisted CVD using hexamethyldisilane, a precursor similar to HMDS, and measured a hardness value of 9±2

GPa, that remained constant with the temperature. Their value is higher than the one measured in the present work, potentially related to their much higher temperature probed (1210-1510°C). It is possible that for small thermal ranges, the hardness values do not variate much, and are possibly more likely linked to the process itself or the precursor chemistry. In fact, recent results for films deposited at similar conditions using a TEOS-O_2/O_3 chemistry (to be published) show that films processed from TEOS have a hardness of approximately 8.0±0.3 GPa. In contrast, literature finds for double-discharge atmospheric pressure CVD of HMDS, plasma polymerized HMDS and PECVD of HMDS resulted in 1.47-3.15, 1.37 and 0.5-3.0 GPa, respectively [78-80]. It is therefore assumed that the change in precursor chemistry, that is, the addition of HMDS, globally degrades the mechanical properties of the film. This is oftentimes correlated to the presence of $–(CH_3)_x$ groups in HMDS films, potential C=C or Si-H bonds, and the resulting film porosity [78-80]. In the present work, even though the transition in material type and presence of $–(CH_3)_x$ has been clearly illustrated though FT-IR and IBA, it seems like the mechanical properties of dual-source HMDS-TEOS films are not as sensitive to compositional changes as other functional properties (i.e. wettability, corrosion resistance, roughness, etc.).

4. Conclusion

Amorphous SiO_x and SiO_xC_y:CH_3 films were prepared by atmospheric pressure thermal CVD using a dual-source chemistry of tetraethyl orthosilicate (TEOS) and hexamethyldisilazane (HMDS). An oxygen-ozone mix played the role of the oxidant and facilitated deposition at relatively low temperatures. The effect of deposition temperature on the composition, chemical structure, wettability and mechanical properties was extensively investigated. FT-IR spectroscopy combined with Ion Beam Analyses and wet etching corrosion tests revealed that the nature of the material transitions from a sacrificial

SiO_xC_y:CH_3 to a more compact SiO_x film with an increase in temperature past 450°C, and vice versa. Additionally, film RMS roughness increases from 0.36 nm up to 4.5 nm with increasing the concentration of $–CH_3$ groups in the films, a spike of both being noted for the transitional temperature of 450°C. The water contact angle increases from 52.8 up to 81.0°, however no spike was observed for that particular temperature, revealing that this surface property is not solely impacted by surface roughness or methylation. For all temperatures, sequential ERDA analysis at the same location on the films systematically revealed hydrogen desorption during the first acquisitions, due to the interaction of the film with the ion beam, with a stronger desorption for the SiO_xC_y:CH_3 films. In light of additional FT-IR results, it was established that methyl moieties originate from the HMDS precursor. It is concluded that a large variety of film properties, with the only exception noted being film hardness, which remained stable within the examined 360-550°C thermal range, can be controlled by the film's composition, and more specifically the carbon content. The latter can in turn be tuned through adjustment of the HMDS flow rate and reactor temperature. An investigation of other process parameters such as oxygen flow rate, along a wider range of HMDS/TEOS ratios, are pathways that should be explored, since they could lead to new combinations of functional properties and potential for application in other sectors.

Acknowledgements

This work was supported by ANR (Agence Nationale de la Recherche) under the contract HEALTHYGLASS ANR-17-CE08-0056. Part of the project was also co-funded by the European Union, the Region – Centre Val de Loire and The French minister of research (MESRI – DRRT). Europe is committed to the Centre-Val de Loire region with the European regional development fund (ERDF). The authors are indebted to Olivier Debieu, Simon

Ponton, Olivier Marsan, Claire Tendero and Claudie Josse for their advice and assistance with ellipsometry, FTIR, AFM and FIB techniques.

References

[1] K. Fujino, Y. Nishimoto, N. Tokumasu, K. Maeda, Silicon Dioxide Deposition by Atmospheric-Pressure and Low-Temperature CVD Using TEOS and Ozone, J. Electrochem. Soc., 137 (1990) 2883-2887.

[2] H. Kotani, M. Matsuura, A. Fujii, H. Genjou, S. Nagao, Low-temperature APCVD oxide using TEOS-ozone chemistry for multilevel interconnections, in: International Technical Digest on Electron Devices Meeting, 1989, pp. 669-672.

[3] J. Chen, Z. Ling, X. Fang, Z. Zhang, Experimental and numerical investigation of form-stable dodecane/hydrophobic fumed silica composite phase change materials for cold energy storage, Energy Convers. Manage., 105 (2015) 817-825.

[4] H. Liang, H. Han, F. Wang, Z. Cheng, B. Lin, Y. Pan, J. Tan, Experimental investigation on spectral splitting of photovoltaic/thermal hybrid system with two-axis sun tracking based on SiO_2/TiO_2 interference thin film, Energy Convers. Manage., 188 (2019) 230-240.

[5] S.-J. Ahn, G.-N. Yun, A. Takagaki, R. Kikuchi, S.T. Oyama, Synthesis and characterization of hydrogen selective silica membranes prepared by chemical vapor deposition of vinyltriethoxysilane, J. Membr. Sci., 550 (2018) 1-8.

[6] V.H. Nguyen, A. Sekkat, C.A. Masse de la Huerta, F. Zoubian, C. Crivello, J. Rubio-Zuazo, M. Jaffal, M. Bonvalot, C. Vallée, O. Aubry, H. Rabat, D. Hong, D. Muñoz-Rojas, Atmospheric Plasma-Enhanced Spatial Chemical Vapor Deposition of SiO_2 Using Trivinylmethoxysilane and Oxygen Plasma, Chem. Mater., 32 (2020) 5153-5161.

[7] M. Nakaya, S. Yasuhara, T. Maeda, A. Hotta, Impact of hot wire and material gas species on the Cat-CVD coating of gas barrier SiOC thin films onto PET bottles, Surf. Coat. Technol., 344 (2018) 21-29.

[8] B.-B. Dong, F.-H. Wang, M.-Y. Yang, J.-L. Yu, L.-Y. Hao, X. Xu, G. Wang, S. Agathopoulos, Polymer-derived porous SiOC ceramic membranes for efficient oil-water separation and membrane distillation, J. Membr. Sci., 579 (2019) 111-119.

[9] K. Akamatsu, M. Suzuki, A. Nakao, S.-i. Nakao, Development of hydrogen-selective dimethoxydimethylsilane-derived silica membranes with thin active separation layer by chemical vapor deposition, J. Membr. Sci., 580 (2019) 268-274.

[10] H. Nagasawa, T. Minamizawa, M. Kanezashi, T. Yoshioka, T. Tsuru, Microporous organosilica membranes for gas separation prepared via PECVD using different O/Si ratio precursors, J. Membr. Sci., 489 (2015) 11-19.

[11] U. Schmid, S. González-Castilla, J. Olivares, M. Clement, L. Vergara, L. Pulido, E. Iborra, J. Sangrador, Silicon oxide sacrificial layers deposited by pulsed-DC magnetron sputtering for MEMS applications, in: Smart Sensors, Actuators, and MEMS IV, 2009.

[12] W. Piyawattanametha, Y.-H. Park, A. Akujärvi, B. Guo, R. Mannila, A. Rissanen, MOEMS FPI sensors for NIR-MIR microspectrometer applications, in: MOEMS and Miniaturized Systems XV, 2016.

[13] M. Modreanu, C. Moldovan, R. Iosub, The etching behavior of APCVD PSG thin films used as sacrificial layers for surface micromachined resonant microstructures, Sens. Actuators, A, 99 (2002) 82-84.

[14] S. Ponton, F. Dhainaut, H. Vergnes, D. Samelor, D. Sadowski, V. Rouessac, H. Lecoq, T. Sauvage, B. Caussat, C. Vahlas, Investigation of the densification mechanisms and corrosion resistance of amorphous silica films, J. Non-Cryst. Solids, 515 (2019) 34-41.

[15] M. Orfert, K. Richter, Plasma enhanced chemical vapor deposition of SiN-films for passivation of three-dimensional substrates, Surf. Coat. Technol., 116-119 (1999) 622-628.

[16] R.G.S. Batocki, R.P. Mota, R.Y. Honda, D.C.R. Santos, Amorphous silicon carbonitride films modified by plasma immersion ion implantation, Vacuum, 107 (2014) 174-177.

[17] A. Jain, Selective and blanket copper chemical vapor deposition for ultra-large-scale integration, J. Vac. Sci. Technol., B: Microelectron. Nanometer Struct., 11 (1993).

[18] S. Kim, J.M. Park, D.J. Choi, The carrier gas and surface passivation effects on selectivity in chemical vapor deposition of copper films, Thin Solid Films, 320 (1998) 95-102.

[19] J.Y. Choi, C.F. Ahles, Y. Cho, A. Anurag, K.T. Wong, S.D. Nemani, E. Yieh, A.C. Kummel, Selective pulsed chemical vapor deposition of water-free HfO_x on Si in preference to SiCOH and passivated SiO_2, Appl. Surf. Sci., 512 (2020).

[20] N.G. Semaltianos, Modification by UV-light irradiation of the affinity for copper chemical vapour deposition of self-assembled monolayers of organosilanes on SiO_2 substrates, Surf. Coat. Technol., 201 (2007) 7327-7338.

[21] H. Nagasawa, Y. Yamamoto, N. Tsuda, M. Kanezashi, T. Yoshioka, T. Tsuru, Atmospheric-pressure plasma-enhanced chemical vapor deposition of microporous silica membranes for gas separation, J. Membr. Sci., 524 (2017) 644-651.

[22] G. Li, G. Zheng, Z. Ding, L. Shi, J. Li, Z. Chen, L. Wang, A.A.O. Tay, W. Zhu, High-performance ultra-low-k fluorine-doped nanoporous organosilica films for inter-layer dielectric, J. Mater. Sci., 54 (2018) 2379-2391.

[23] K.-S. Park, Y. Kim, Processing of SiO_2 Protective Layer Using HMDS Precursor by Combustion CVD, J. Nanosci. Nanotechnol., 11 (2011) 7265-7268.

[24] M.E. Coltrin, P. Ho, H.K. Moffat, R.J. Buss, Chemical kinetics in chemical vapor deposition: growth of silicon dioxide from tetraethoxysilane (TEOS), Thin Solid Films, 365 (2000) 251-263.

[25] A. Walkiewicz-Pietrzykowska, J. Cotrino, A.R. González-Elipe, Deposition of Thin Films of SiOxCyH in a Surfatron Microwave Plasma Reactor with Hexamethyldisiloxane as Precursor, Chem. Vap. Deposition, 11 (2005) 317-323.

[26] Y.S. Kim, J.H. Lee, J.T. Lim, J.B. Park, G.Y. Yeom, Atmospheric pressure PECVD of SiO_2 thin film at a low temperature using HMDS/O_2/He/Ar, Thin Solid Films, 517 (2009) 4065-4069.

[27] J.P. Nieto, L. Jeannerot, B. Caussat, Modelling of an industrial moving belt chemical vapour deposition reactor forming SiO_2 films, Chem. Eng. Sci., 60 (2005) 5331-5340.

[28] K. Nakamura, H. Nonaka, N. Kameda, T. Nishiguchi, S. Ichimura, Photochemical Reaction of Ozone and 1,1,1,3,3,3-Hexamethyldisilazane: Analysis of the Gas Reaction between Precursors in a Photochemical Vapor Deposition Process, Jpn. J. Appl. Phys., 47 (2008) 7349-7355.

[29] J.K. Choi, D.H. Kim, J. Lee, J.B. Yoo, Effects of process parameters on the growth of thick SiO_2 using plasma enhanced chemical vapor deposition with hexamethyldisilazane, Surf. Coat. Technol., 131 (2000) 136-140.

[30] V.K. Tomar, D.K. Gautam, Deposition and characterization of Si-rich silicon oxide films using HMDS for integrated photonics, Mater. Sci. Semicond. Process., 10 (2007) 200-205.

[31] S.W. Benson, A.E. Axworthy, Mechanism of the Gas Phase, Thermal Decomposition of Ozone, J. Chem. Phys., 26 (1957) 1718-1726.

[32] K.C. Topka, G.A. Chliavoras, F. Senocq, H. Vergnes, D. Samelor, D. Sadowski, C. Vahlas, B. Caussat, Large temperature range model for the atmospheric pressure chemical vapor deposition of silicon dioxide films on thermosensitive substrates, Chem. Eng. Res. Des., 161 (2020) 146-158.

[33] P. Lange, W. Windbracke, Characterization of Thermal and Deposited Thin Oxide Layers by Longitudinal Optical-Transverse Optical-Excitation in Fourier-Transform Ir Transmission Measurements, Thin Solid Films, 174 (1989) 159-164.

[34] C. Martinet, R.A.B. Devine, Analysis of the vibrational mode spectra of amorphous SiO_2 films, J. Appl. Phys., 77 (1995) 4343-4348.

[35] M. Mayer, SIMNRA, a simulation program for the analysis of NRA, RBS and ERDA, AIP Conf. Proc., 475 (1999) 541-544.

[36] W.C. Oliver, G.M. Pharr, An improved technique for determining hardness and elastic modulus using load and displacement sensing indentation experiments, J. Mater. Res., 7 (2011) 1564-1583.

[37] T. Young, III. An essay on the cohesion of fluids, Philos. Trans. R. Soc. London, 95 (1805) 65-87.

[38] R.N. Wenzel, Surface Roughness and Contact Angle, J. Phys. Colloid Chem., 53 (1949) 1466-1467.

[39] W.A. Pliskin, R.P. Gnall, Evidence for Oxidation Growth at the Oxide-Silicon Interface from Controlled Etch Studies, J. Electrochem. Soc., 111 (1964) 872.

[40] W.A. Pliskin, Comparison of properties of dielectric films deposited by various methods, J. Vac. Sci. Technol., 14 (1977) 1064-1081.

[41] L.D. Flores, J.E. Crowell, Boundary layer chemistry probed by in situ infrared spectroscopy during SiO_2 deposition at atmospheric pressure from tetraethylorthosilicate and ozone, J. Phys. Chem. B, 109 (2005) 16544-16553.

[42] S. Nguyen, D. Dobuzinsky, D. Harmon, R. Gleason, S. Fridmann, Reaction-Mechanisms of Plasma-Assisted and Thermal-Assisted Chemical Vapor-Deposition of Tetraethylorthosilicate Oxide-Films, J. Electrochem. Soc., 137 (1990) 2209-2215.

[43] E.J. Kim, W.N. Gill, Analytical Model for Chemical-Vapor-Deposition of SiO_2-Films Using Tetraethoxysilane and Ozone, J. Cryst. Growth, 140 (1994) 315-326.

[44] E. Gil, J.B. Park, J.S. Oh, G.Y. Yeom, Characteristics of SiOx thin films deposited by atmospheric pressure chemical vapor deposition as a function of HMDS/O_2 flow rate, Thin Solid Films, 518 (2010) 6403-6407.

[45] S.N. Taraskin, S.R. Elliott, Nature of vibrational excitations in vitreous silica, Phys. Rev. B, 56 (1997) 8605-8622.

[46] P. Innocenzi, P. Falcaro, D. Grosso, F. Babonneau, Order-disorder transitions and evolution of silica structure in self-assembled mesostructured silica films studied through FTIR spectroscopy, J. Phys. Chem. B, 107 (2003) 4711-4717.

[47] T.M. Parrill, Transmission infrared study of acid-catalyzed sol-gel silica coatings during room ambient drying, J. Mater. Res., 7 (2011) 2230-2239.

[48] P. Lange, Evidence for disorder-induced vibrational mode coupling in thin amorphous SiO_2 films, J. Appl. Phys., 66 (1989) 201-204.

[49] S. Bulou, L. Le Brizoual, P. Miska, L. de Poucques, R. Hugon, M. Belmahi, J. Bougdira, The influence of CH_4 addition on composition, structure and optical characteristics of SiCN thin films deposited in a CH_4/N_2/Ar/hexamethyldisilazane microwave plasma, Thin Solid Films, 520 (2011) 245-250.

[50] H. Nagasawa, Y. Yamamoto, M. Kanezashi, T. Tsuru, Atmospheric-Pressure Plasma-Enhanced Chemical Vapor Deposition of Hybrid Silica Membranes, J. Chem. Eng. Jpn., 51 (2018) 732-739.

[51] F. Benitez, E. Martinez, J. Esteve, Improvement of hardness in plasma polymerized hexamethyldisiloxane coatings by silica-like surface modification, Thin Solid Films, 377 (2000) 109-114.

[52] P.H.T. Ngamou, J.P. Overbeek, R. Kreiter, H.M. van Veen, J.F. Vente, I.M. Wienk, P.F. Cuperus, M. Creatore, Plasma-deposited hybrid silica membranes with a controlled retention of organic bridges, J. Mater. Chem. A, 1 (2013).

[53] J.H. Lee, C.H. Jeong, J.T. Lim, V.A. Zavaleyev, S.J. Kyung, G.Y. Yeom, SiO_xN_y thin film deposited by plasma enhanced chemical vapor deposition at low temperature using HMDS–O_2–NH_3–Ar gas mixtures, Surf. Coat. Technol., 201 (2007) 4957-4960.

[54] W.K. Choi, L.P. Lee, S.L. Foo, S. Gangadharan, N.B. Chong, L.S. Tan, Oxidation study of plasma-enhanced chemical vapor deposited and rf sputtered hydrogenated amorphous silicon carbide films, J. Appl. Phys., 89 (2001).

[55] M.I. Baraton, M.S. ElShall, Synthesis and characterization of nanoscale metal oxides and carbides .2. Micro-Raman and FT-IR surface studies of a silicon carbide powder, Nanostruct. Mater., 6 (1995) 301-304.

[56] G. Ramis, P. Quintard, M. Cauchetier, G. Busca, V. Lorenzelli, Surface-Chemistry and Structure of Ultrafine Silicon-Carbide - an Ft-Ir Study, J. Am. Ceram. Soc., 72 (1989) 1692-1697.

[57] Q. Chen, Y. Zhang, E. Han, Y. Ge, SiO_2-like film deposition by dielectric barrier discharge plasma gun at ambient temperature under an atmospheric pressure, J. Vac. Sci. Technol. A, 24 (2006) 2082-2086.

[58] K. Schmidt-Szalowski, Z. Rżanek-Boroch, J. Sentek, Z. Rymuza, Z. Kusznierewicz, M. Misiak, Thin Films Deposition from Hexamethyldisiloxane and Hexamethyldisilazane under Dielectric-Barrier Discharge (DBD) Conditions, Plasmas Polym., 5 (2000) 173-190.

[59] D. Trunec, Z. Navrátil, P. Stahel, L. Zají ková, V. Bur íková, J. Cech, Deposition of thin organosilicon polymer films in atmospheric pressure glow discharge, J. Phys. D: Appl. Phys., 37 (2004) 2112-2120.

[60] D.M. Dobkin, S. Mokhtari, M. Schmidt, A. Pant, L. Robinson, A. Sherman, Mechanisms of Deposition of SiO_2 from TEOS and Related Organosilicon Compounds and Ozone, J. Electrochem. Soc., 142 (1995) 2332-2340.

[61] F. Massines, N. Gherardi, A. Fornelli, S. Martin, Atmospheric pressure plasma deposition of thin films by Townsend dielectric barrier discharge, Surf. Coat. Technol., 200 (2005) 1855-1861.

[62] J. Gope, S. Kumar, S. Singh, C.M.S. Rauthan, P.C. Srivastava, Growth of Mixed-Phase Amorphous and Ultra Nanocrystalline Silicon Thin Films in the Low Pressure Regime by a VHF PECVD Process, Silicon, 4 (2012) 127-135.

[63] A. Milella, F. Palumbo, J.L. Delattre, F. Fracassi, R. d'Agostino, Deposition and Characterization of Dielectric Thin Films from Allyltrimethylsilane Glow Discharges, Plasma Processes Polym., 4 (2007) 425-432.

[64] F.X.L.i. Xamena, A. Zecchina, FTIR spectroscopy of carbon dioxide adsorbed on sodium- and magnesium-exchanged ETS-10 molecular sieves, Phys. Chem. Chem. Phys., 4 (2002) 1978-1982.

[65] R.W. Stevens, R.V. Siriwardane, J. Logan, In situ Fourier transform infrared (FTIR) investigation of CO_2 adsorption onto zeolite materials, Energy Fuels, 22 (2008) 3070-3079.

[66] M.S. Haque, H.A. Naseem, W.D. Brown, Characterization of High-Rate Deposited PECVD Silicon Dioxide Films for Mcm Applications, J. Electrochem. Soc., 142 (1995) 3864-3869.

[67] P. Innocenzi, Infrared spectroscopy of sol-gel derived silica-based films: a spectra-microstructure overview, J. Non-Cryst. Solids, 316 (2003) 309-319.

[68] J.T. Fitch, Effects of thermal history on stress-related properties of very thin films of thermally grown silicon dioxide, J. Vac. Sci. Technol. B, 7 (1989).

[69] N. Primeau, C. Vautey, M. Langlet, The effect of thermal annealing on aerosol-gel deposited SiO_2 films: a FTIR deconvolution study, Thin Solid Films, 310 (1997) 47-56.

[70] V.E. Vamvakas, D. Davazoglou, Comparison of FTIR Transmission Spectra of Thermally and LPCVD SiO_2 Films Grown by TEOS Pyrolysis, J. Electrochem. Soc., 151 (2004).

[71] R.N. Wenzel, Resistance of solid surfaces to wetting by water, Ind. Eng. Chem., 28 (1936) 988-994.

[72] T.-Y. Lo, Y.-C. Huang, Y.-N. Hsiao, C.-G. Chao, W.-T. Whang, Preparation of superhydrophobic polyimide films modified with organosilicasol as effective anticorrosion coatings, Surf. Coat. Technol., 258 (2014) 310-319.

[73] D. Lai, G. Kong, C. Che, Synthesis and corrosion behavior of ZnO/SiO_2 nanorod-sub microtube superhydrophobic coating on zinc substrate, Surf. Coat. Technol., 315 (2017) 509-518.

[74] Y.-S. Wei, W.-Y. Liu, H.-M. Wu, K.-S. Chen, V. Cech, Characteristics of SiO_x-containing hard film prepared by low temperature plasma enhanced chemical vapor deposition using hexamethyldisilazane or vinyltrimethylsilane and post oxygen plasma treatment, Mater. Chem. Phys., 189 (2017) 183-190.

[75] D.M. Knotter, Etching mechanism of vitreous silicon dioxide in HF-based solutions, J. Am. Chem. Soc., 122 (2000) 4345-4351.

[76] Y. Shioya, H. Shimoda, K. Maeda, T. Ohdaira, R. Suzuki, Y. Seino, Low-k SiOCH Film Deposited by Plasma-Enhanced Chemical Vapor Deposition Using Hexamethyldisiloxane and Water Vapor, Jpn. J. Appl. Phys., 44 (2005) 3879-3884.

[77] I.S. Merenkov, H. Katsui, M.N. Khomyakov, V.S. Sulyaeva, R.V. Pushkarev, R. Tu, T. Goto, M.L. Kosinova, Extraordinary synergetic effect of precursors in laser CVD deposition of SiBCN films, J. Eur. Ceram. Soc., 39 (2019) 5123-5131.

[78] J. Park, J. Oh, E. Gil, G.Y. Yeom, Characteristics of SiOX thin films deposited by atmospheric pressure chemical vapor deposition using a double-discharge system, Mater. Res. Bull., 47 (2012) 3011-3014.

[79] C. Shim, D. Jung, Relationship between C=C Bonds and Mechanical Properties of Carbon Rich Low-k Films deposited by Plasma Enhanced Chemical Vapor Deposition, Jpn. J. Appl. Phys., 43 (2004) 940-944.

[80] R.Y. Honda, R.P. Mota, R.G.S. Batocki, D.C.R. Santos, T. Nicoleti, K.G. Kostov, M.E. Kayama, M.A. Algatti, N.C. Cruz, L. Ruggiero, Plasma-polymerized hexamethyldisilazane treated by nitrogen plasma immersion ion implantation technique, J. Phys., 167 (2009) 012055.